



# Multi-Pinhole Based X-Ray Fluorescence Computed Tomography: A Comparison with Single Pinhole Case

Tenta Sasaya<sup>1</sup>, Naoki Sunaguchi<sup>2</sup>, Seung-Jun Seo<sup>3</sup>, Tsutomu Zeniya<sup>4</sup>,  
Kazuyuki Hyodo<sup>5</sup>, Jong-Ki Kim<sup>3</sup>, and Tetsuya Yuasa<sup>1(✉)</sup>

<sup>1</sup> Yamagata University, Yonezawa 992-8510, Japan  
yuasa@yz.yamagata-u.ac.jp

<sup>2</sup> Nagoya University, Nagoya 461-8673, Japan

<sup>3</sup> Catholic University of Daegu, Daegu 705-034, Korea

<sup>4</sup> Hirosaki University, Hirosaki 036-8560, Japan

<sup>5</sup> High Energy Accelerator Organization, Tsukuba 305-0035, Japan

**Abstract.** An x-ray fluorescence computed tomography using a pinhole collimator (p-XFCT) for medical use depicts the 3-D distribution of imaging agent by collecting the x-ray fluorescence photons emitted from the imaging agent accumulated in an organ using a pinhole collimator and a 2-D detector. However, the number of the fluorescent x-ray photons are restricted by the pinhole, leading to acquisition of low *S/N* projections due to the photon starvation. Simultaneous acquisition of multiple projections using a multi-pinhole scheme overcomes the photon starvation. In this research, we clarified the measurement process and described the quantitative linear relationship between the quantities to be estimated and to be measured. We solved the multi-pinhole based XFCT (mp-XFCT) as a linear inverse problem regarding the described measurement process using ML-EM (maximum likelihood expectation-maximization) algorithm. We actually constructed an mp-XFCT imaging system at beamline AR-NE7A in KEK, and performed imaging experiment using a physical phantom to demonstrate the efficacy of mp-XFCT.

**Keywords:** X-ray fluorescence · Computed tomography · Pinhole · Molecular imaging

## 1 Introduction

In preclinical research, rodent models of human diseases yielded by genetic and tissue engineering are frequently used for elucidating their causes and developing their diagnosis and treatment. Nuclear imaging techniques such as positron emission tomography (PET) and single photon emission computed tomography (SPECT) are very important tools for *in vivo* observing functional information of the organs, *i.e.*, the physiological and pathological characteristics, from the molecular viewpoint. However, they require radioactive imaging agents, leading to the measurement difficulty. Thus, a novel molecular imaging technique using non-radioactive imaging agents would be advantageous.

Combining x-ray fluorescence analysis, which is one of the most sensitive physico-chemical analysis, with computed tomography, which provides the 3-D information, enables us to establish a low-invasive or nondestructive molecular imaging technique. So far, several types of the x-ray fluorescence computed tomography (XFCT) imaging scheme have been proposed [1–14]. Among them a pinhole based XFCT (p-XFCT) outperforms the others in establishing both spatial resolution and fast scanning [13]. However, since the number of detected fluorescent photons are remarkably restricted by a pinhole, leading to acquisition of low S/N projections due to the photon starvation. Use of multiple pinholes simultaneously collects multiple projections, and then compensates the photon starvation effect [16, 17]. In this research, we clarified the measurement process of the multi-pinhole based XFCT (mp-XFCT) required for reconstruction. We actually constructed the mp-XFCT imaging system at beamline AR-NE7A in KEK, and performed an imaging experiment using a physical phantom to demonstrate the efficacy of mp-XFCT.

## 2 Method

### 2.1 Multi-Pinhole Based XFCT

Figure 1 shows the imaging geometry of mp-XFCT, which has seven pinholes, within the  $xyz$ -coordinate system. A monochromatic and parallel incident beam propagates along the  $x$ -axis, and a pinhole collimator is set so that its surface is perpendicular to the  $z$ -axis and the center of the pinhole lies on the  $z$ -axis. The surface of a two-dimensional detector is set perpendicular to the  $z$ -axis. The volumetric incident beam irradiates an object positioned in the vicinity of the origin, with the volumetric beam covering the object. Imaging agents in the object, such as I, Gd, and Au, are excited by the incident beam and isotropically emit fluorescent x-ray photons on de-excitation. Of all the fluorescent x-ray photons emitted from all of the imaging agents in the object, only the photons passing through the pinholes are acquired by the detector. Each view produces multiple projections corresponding to the individual pinholes. The projection acquisition is repeated while rotating the object around the  $y$ -axis. In the following, we assume that  $K_{\alpha 1}$  fluorescence is dominant, although other fluorescents such as  $K_{\alpha 2}$  and  $K_{\beta}$ , can easily be incorporated into the subsequent expressions, despite a more complicated formulation.

### 2.2 Measurement Process for a Single Pinhole

Let us consider quantitatively how the fluorescent x-ray photons are detected at an element on the detective surface for a single pinhole. As shown in Fig. 1, consider a point  $Q$  inside the object on an incident x-ray flux, and a point  $S$  at the center of the detective element. We assume that point  $P$  is an intersection of the incident flux and the object surface, point  $Q$  is an intersection of the incident flux and the line connecting  $S$  to the pinhole center, and point  $R$  is an intersection of a line connecting  $Q$  to  $S$  and the object surface.

First, we will consider the measurement process when the above assumption holds. The process is divided into the following three subprocesses:

- (a) attenuation of the incident beam by the object from  $P$  to  $Q$ ;
- (b) emission of fluorescent x-rays at  $Q$ ; and
- (c) attenuation of the fluorescent x-rays by the object from  $Q$  to  $R$ , which then travel to  $S$ .

In subprocess (a), the density of incident x-ray photons having reached  $Q$  is given as  $I_{(a)}(\mathbf{r}_Q) = I_0 t \exp(-\int_{\overline{PQ}} \mu_a(E_I, \mathbf{r}) dl)$  [photons/mm<sup>2</sup>] owing to attenuation in line segment  $\overline{PQ}$ , where  $\mathbf{r}_Q$  is the coordinate of  $Q$ ,  $I_0$  [photons/mm<sup>2</sup>/s] is the number of incident photons per unit area and time,  $E_I$  [keV], and  $\mu_a(E, \mathbf{r})$  [1/mm] are the energy of incident x-ray and the three-dimensional map of the linear total attenuation coefficient inside the object at incident energy  $E$ , respectively, and  $t$ [s] is the exposure time.

In subprocess (b), the quantity of fluorescent x-rays emitted at  $Q$  is proportional to the product of the incident photon density  $I_{(a)}(\mathbf{r}_Q)$  [photons/mm<sup>2</sup>] and the concentration of imaging element  $\lambda(\mathbf{r}_Q)$  [g/mm<sup>3</sup>], given as  $I_{(b)}(\mathbf{r}_Q) = \mu_{ph} \omega I_{(a)}(\mathbf{r}_Q) \lambda(\mathbf{r}_Q) \Delta\mathbf{r}_Q$  [photons], where  $\mu_{ph}$  [mm<sup>2</sup>/g] and  $\omega$  are the photoelectric mass absorption coefficient of trace element and fluorescent yield, respectively, and  $\Delta\mathbf{r}_Q$  [mm<sup>3</sup>] is an infinitesimal volume in the vicinity of  $Q$ .

In subprocess (c), of all the fluorescent x-ray fluxes emitted isotropically from  $Q$ , only the fluxes passing through the pinhole reach the detector, and the passing fluorescent fluxes are attenuated by the object. This attenuation is represented by the attenuation in the line segment  $\overline{QR}$ , as the area of the pinhole is sufficiently small, although actually each flux is differently attenuated according to the propagation direction. Therefore, the fluorescent quantity emitted from  $Q$  and reaching  $S$  is given by  $I_{(c)}(\mathbf{r}_S, \mathbf{r}_Q) = I_{(b)}(\mathbf{r}_Q) (\Omega(\mathbf{r}_S, \mathbf{r}_Q)/4\pi) \exp(-\int_{\overline{QR}} \mu_a(E_F, \mathbf{r}) dl)$  [photons], where  $\mathbf{r}_S$  is the coordinate of  $S$ ,  $\Omega(\mathbf{r}_S, \mathbf{r}_Q)$  [steradian] and  $E_F$  [keV] are the solid angle subtended by  $Q$  through the pinhole toward the detective element whose center is  $S$ , and the energy of the fluorescent x-ray, respectively. For the subsequent discussion, we denote the fluorescent x-ray photons that are counted at the detective element at the coordinate whose center is  $\mathbf{r}_S$  as

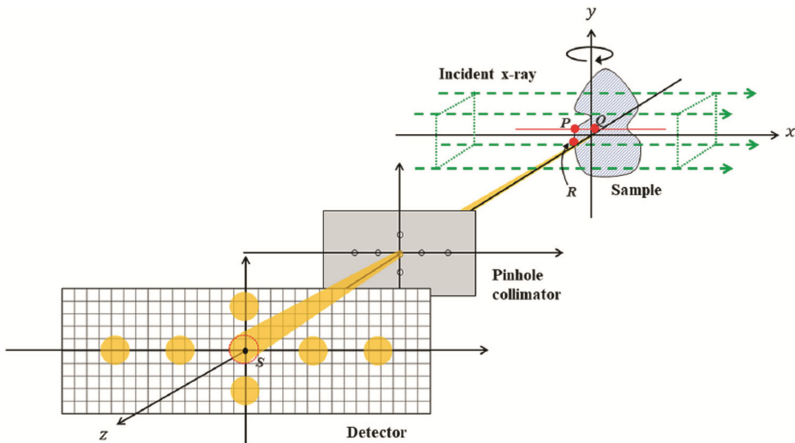


**Fig. 1.** Schematic of multi-pinhole based x-ray fluorescent computed tomography.

$$I_{(c)}(\mathbf{r}_S, \mathbf{r}_Q) = p(\mathbf{r}_S, \mathbf{r}_Q) \lambda(\mathbf{r}_Q) \Delta \mathbf{r}_Q, \quad (1)$$

where

$$p(\mathbf{r}_S, \mathbf{r}_Q) = \eta \mu_{pr} \omega I_0 t / 4\pi \exp\left(-\int_{PQ} \mu_a(E_I, \mathbf{r}) dl - \int_{QR} \mu_a(E_F, \mathbf{r}) dl\right) \Omega(\mathbf{r}_S, \mathbf{r}_Q) \quad (2)$$

and  $\eta$  is the quantum efficiency of the detector. If we specify the imaging geometry and the coordinates of  $S$  and  $Q$ ,  $p(\mathbf{r}_S, \mathbf{r}_Q)$  can be known in advance, as the maps of  $\mu_a(E_I, \mathbf{r})$  and  $\mu_a(E_F, \mathbf{r})$  can be measured by ordinary computed tomography with monochromatic x-rays.

The above discussion concerns the contribution of fluorescent x-ray counts at  $S$  from  $Q$ , although the contributions from all regions around  $Q$  should actually be considered. Therefore, the total measured count at  $S$  is given as

$$y(\mathbf{r}_S) = \iiint_{V_S} p(\mathbf{r}_S, \mathbf{r}_Q) \lambda(\mathbf{r}_Q) d\mathbf{r}_Q, \quad (3)$$

where  $V_S$  is a region in the object inside a cone subtended by  $S$  toward the pinhole.

For reconstruction, we discretize the object with voxels as shown in Fig. 2. Here we assume that in the projection acquisition process, the object is fixed to the  $xyz$ -coordinate system, and that the incident beam, the pinhole collimator, and the detective surface are rotated around the  $y$ -axis, with their positional relationship maintained, although in the actual measurement the object is rotated. We introduce the index  $j$  ( $= 1, 2, \dots, N$ ) to identify the voxel in the lexicographic ordering corresponding to  $\mathbf{r}_Q$ , where  $N$  is the number of voxels. Additionally, we introduce the index  $i$  ( $= 1, 2, \dots, M$ ) to identify the position of the individual detective elements throughout the whole projection acquisition, corresponding to  $\mathbf{r}_S$ , where the positions of detective elements throughout the whole projection acquisition are consecutively numbered, and  $M$  is the number of the positions. As a result, Eq. (3) is discretized to

$$y_i = \sum_{j \in V_i} p_{ij} \lambda_j \quad (i = 1, 2, \dots, M), \quad (4)$$

where  $y_i, p_{ij}, V_i$  and  $\lambda_j$  correspond to  $y(\mathbf{r}_S), p(\mathbf{r}_S, \mathbf{r}_Q) \Delta \mathbf{r}_Q, V_S$  and  $\lambda(\mathbf{r}_Q)$ , respectively.  $y_i$  and  $p_{ij}$  are known, and  $\lambda_j$  requires estimation.

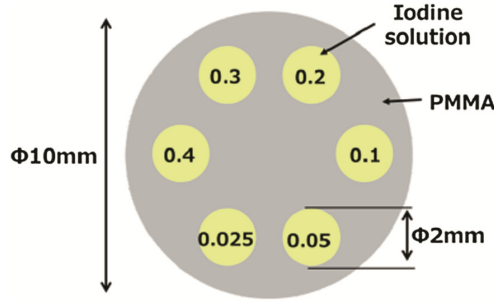


**Fig. 2.** Cross section of a physical phantom, which has six channels filled with different concentrations of I (0.025, 0.05, 0.1, 0.2, 0.3, 0.4 I mg/ml).

### 2.3 Reconstruction for Multi-pinhole XFCT

Since use of a multi-pinhole collimator produces projections for the individual pinholes, Eq. (1) is rewritten as

$$y_i^k = \sum_j p_{ij}^k \lambda_j^k \quad (i = 1, 2, \dots, M; k = 1, 2, \dots, L), \quad (5)$$

where  $k$  is an index to identify the pinhole and  $L$  is the number of pinholes. As a result, we obtain a system of  $M \times L$  linear equations. Then, we obtain  $L$  matrix equations  $\mathbf{y}^k = \mathbf{P}^k \boldsymbol{\lambda}$  ( $1 \leq k \leq L$ ), where  $\mathbf{y}^k = (y_1^k, y_2^k, \dots, y_M^k)^T$ ,  $\boldsymbol{\lambda} = (\lambda_1, \lambda_2, \dots, \lambda_N)^T$ , and

$$\mathbf{P}^k = \begin{pmatrix} p_{11}^k & p_{12}^k & \cdots & p_{1N}^k \\ p_{21}^k & \ddots & & p_{2N}^k \\ \vdots & & \ddots & \vdots \\ p_{M1}^k & p_{M2}^k & \cdots & p_{MN}^k \end{pmatrix}.$$

In addition, we introduce a  $K (= L \times M)$ -dimensional vector  $\boldsymbol{\psi}$  and a  $K \times N$  matrix  $\boldsymbol{\Pi}$ , where

$$\boldsymbol{\psi} = (y_1^1, y_2^1, \dots, y_M^1, y_1^2, y_2^2, \dots, y_M^2, \dots, y_1^L, y_2^L, \dots, y_M^L)^T$$

, and

$$\boldsymbol{\Pi} = \begin{pmatrix} \mathbf{P}^1 \\ \mathbf{P}^2 \\ \vdots \\ \mathbf{P}^L \end{pmatrix}.$$

As a result, a linear inverse problem,

$$\boldsymbol{\psi} = \boldsymbol{\Pi} \boldsymbol{\lambda}, \quad (6)$$

should be solved, where vector  $\boldsymbol{\psi}$  and matrix  $\mathbf{\Pi}$  are known, and vector  $\boldsymbol{\lambda}$  is to be estimated. For reconstruction, we straightforwardly applied the maximum likelihood expectation-maximization (ML-EM) algorithm to our linear inverse problem,  $\boldsymbol{\psi} = \mathbf{\Pi}\boldsymbol{\lambda}$  [18, 19].

### 3 Experiment and Result

We constructed the mp-FXCT imaging system using the bending-magnet beamline AR-NE7A (6.5 GeV) at KEK. Since in this research we paid attention to K-shell fluorescence of I ( $K_{\alpha 1}$ : 28.3 keV), we by a double-crystal Bragg-Bragg monochromator using Si (111) single crystals selected the incident energy to 33.4 keV just above the K-edge energy of I (33.2 keV), so that we can generate as many fluorescent photons as possible. The flux rate was about  $5.0 \times 10^8$  photons/mm<sup>2</sup>/s in front of the object. The cross section of the incident beam was collimated to 35 mm (horizontal)  $\times$  5 mm (vertical) by the slit.

A Pilatus 100 K with  $487 \times 195$  elements (pixel size:  $172 \times 172 \mu\text{m}^2$ ) manufactured by DECTRIS Ltd. was used [15–17]. This detector was used because it offers a high signal-to-noise ratio thanks to no dark current, and it also offers a higher data transmission rate than other types of 2-D detectors, such as CCD-based detectors.

We fabricated a multi-pinhole collimator with 15 pinholes aligned in three rows containing five pinholes each. The collimator consisted of a 1-mm-thick PB plate and 15 W pinhole tips [16]. Each pinhole tip had a 0.1-mm-diameter hole. The pinholes were arranged so that the projections would not overlap.

The distance between the sample rotational axis and the collimator plane, and between the collimator plane and the detector surface were 27.8 mm, and 32.2 mm, respectively. The rotational stage and the detector were controlled by a PC.

We prepared a physical phantom which is a 10-mm-diameter PMMA made cylinder with six 2-mm-diameter channels filled with different concentrations of I solution (0.012, 0.025, 0.005, 0.1, 0.2, 0.3 I mg/ml), as shown in Fig. 2. The phantom was imaged with the exposure time per view of 2 min. 180 projections were obtained at a constant angular step of 2 degrees over 360 degrees.

We solved the inverse problem using the ordered subsets expectation maximization (OSEM) method which is an accelerated version of ML-EM and used widely in PET and SPECT reconstruction [18, 19]. The algorithm was implemented using C# on a PC with Windows 7, Intel Xeon CPU E5-2620, and 192 GB of memory. We set the number of subsets and of iterations were 3 and 5, respectively. The voxel size was  $70 \times 70 \times 40$ ; An edge of a voxel was 0.172 mm long, which is the same as the pixel dimension of the Pilatus detector.

Figure 3 depicts cross-sections acquired at the central levels of the 3-D reconstructed images (a) and their 3-D volume rendering images (b), where the left and right columns were reconstructed using a single pinhole and 15 pinholes, respectively. The back ground is noisier and the I-containing regions are less smooth in single-pinhole case than in the multi-pinhole case.

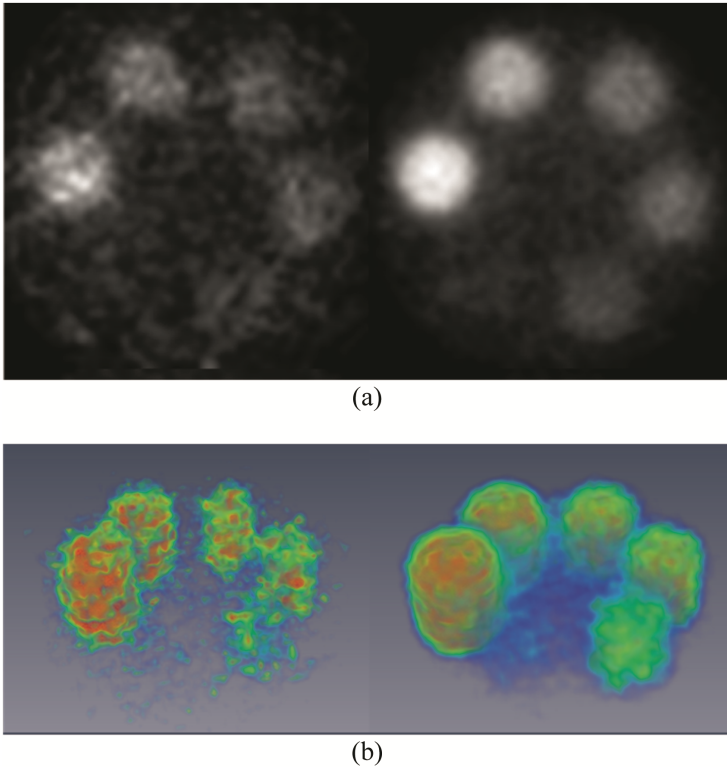


**Fig. 3.** Reconstructed images: (a) the cross sectional images by p-XFCT (left) and mp-XFCT (right), (b) the volume rendering images by p-XFCT (left) and mp-XFCT (right).

## 4 Conclusion

We described the imaging principle of multi-pinhole based x-ray fluorescence computed tomography (mp-XFCT) from the viewpoint of the measurement process. Then, we performed a phantom imaging experiment using an actual imaging system constructed in AR-NE7A and compare the result with the result in a single pinhole case to demonstrate that mp-XFCT improve an image quality by compensating the photon starvation effect caused by a pinhole.

In the present reconstruction process, scatter correction was not incorporated. In the experiment, the phantom size was relatively small, and then scatter components can be neglected. However, in a case of measuring a small animal much more scatter events will occur. Our future direction will be to devise the scatter correction and incorporate it with the reconstruction algorithm.

## References

1. Cesareo, R., et al.: Nucl. Instrum. Meth. A **277**, 559–672 (1989)
2. Hogan, J.P., et al.: IEEE Trans. Nucl. Sci. **38**, 1721–1727 (1991)
3. Schroer, C.G.: Appl. Phys. Lett. **79**, 1912–1914 (2001)
4. Glosio, B., et al.: J. Appl. Phys. **94**, 145–156 (2003)
5. Rust, G.F., et al.: IEEE Trans. Nucl. Sci. **45**, 75–88 (1998)
6. Yuasa, T., et al.: IEEE Trans. Nucl. Sci. **44**, 54–62 (1997)
7. Yuasa, T., et al.: IEEE Trans. Nucl. Sci. **44**, 1760–1769 (1997)
8. Huo, Q., et al.: Opt. Lett. **33**, 2494–2496 (2008)
9. Huo, Q., et al.: X-Ray Spectrosc. **38**, 439–445 (2009)
10. Takeda, T., et al.: J. Synchrotron Radiat. **16**, 57–62 (2009)
11. Lwin, T.T., et al.: J. Synchrotron Radiat. **14**, 158–162 (2007)
12. Lwin, T.T., et al.: J. Synchrotron Radiat. **15**, 528–531 (2008)
13. Sunaguchi, N., et al.: Opt. Comm. **297**, 210–215 (2013)
14. Bazalova-Carter, M., et al.: Radiother. Oncol. **15**, S66–S57 (2015)
15. Sasaya, T., et al.: Sci. Rep. **7**, 44143 (2017)
16. Sasaya, T., et al.: Sci. Rep. **7**, 5742 (2017)
17. Sasaya, T., et al.: Nucl. Instrum. Meth. A **886**, 71–76 (2018)
18. Lange, K., Garson, R.: J. Comput. Assist. Tomogr. **8**, 306–316 (1984)
19. Shepp, L.A., Vardi, V.: IEEE Trans. Med. Imaging **1**, 113–121 (1982)